Journal of Sound and Vibration (2001) **256**(5), 969–979
doi:10.1006/jsvi.2001.4226, available online at http://www.idealibrary.com on IDEAL®

LETTERS TO THE EDITORS

ON THE EFFECT OF TIME SCALING ON THE NOISE RADIATED BY AN ENGINE PLUME

A. Frendi

Mechanical and Aerospace Engineering Department, University of Alabama Huntsville, Huntsville, AL 35899, *U.S.A.*

AND

T. Nesman and T.-S. Wang

NASA Marshall Space Flight Center, Huntsville, AL 35899, *U.S.A.*

(*Received* 5 *July* 2001, *and in final form* 26 *November* 2001)

1. INTRODUCTION

The most important contribution to jet noise studies is due to Lighthill [1, 2], who used the basic fluid dynamic equations to derive the well-known Lighthill acoustic analogy. This equation gives the sound pressure at a farfield point radiated by a localized unsteady source or turbulent flow. Ribner [3] used the Lighthill acoustic analogy to arrive at a relation between the mean-square pressure radiated by a jet plume into the far field as the integral over the plume volume of quadrupole correlations. Ribner [4, 5] also showed the importance of convection and refraction on the farfield jet noise. Several other significant contributions to jet noise theory have been made by various researchers and are summarized in the review papers by Ffowcs Williams [6, 7], Goldstein [8] and Tam [9].

Mani *et al.* [10] used Ribner [3] and Ffowcs Williams' [11] jet noise models in their extensive studies on high-velocity jet noise. Good agreement was obtained between the model and the experimental results for various nozzle geometries and flow regimes. More recently, Frendi *et al.* [12] used a $(k-\varepsilon)$ turbulence model to compute the noise generated by the X-33 linear aerospike engine. They used the Mani *et al.* [10] approach to arrive at their results. Comparisons with experiments showed good agreement. Other computational studies using the $(k-\varepsilon)$ turbulence model were carried out (for example references [13–15]) with varying degrees of success. Recently, Tam *et al.* [16] proposed a self-contained, semi-empirical jet noise theory for the prediction of fine-scale turbulence noise from high-speed jets. The theory uses jet flow turbulence information supplied by a $(k-\varepsilon)$ turbulence model. In addition to the empirical constants found in the turbulence model, three empirical constants were added in the proposed jet noise theory. Noise predictions obtained from the new theory were in excellent agreement with measurements. The new theory uses linearized Euler equations to determine the farfield acoustic pressure, which is a departure from the widely used Lighthill acoustic analogy.

In all the above studies, a time and length scale is specified in the model. The most widely used time scale is that proportional to k/ε. In this paper, three different time scales proportional to $(\partial U/\partial n)^{-1}$, k/ε and k/Pr are tested. In addition, a new acoustic radiation

0022-460X/02/$35.00 © 2002 Elsevier Science Ltd. All rights reserved.

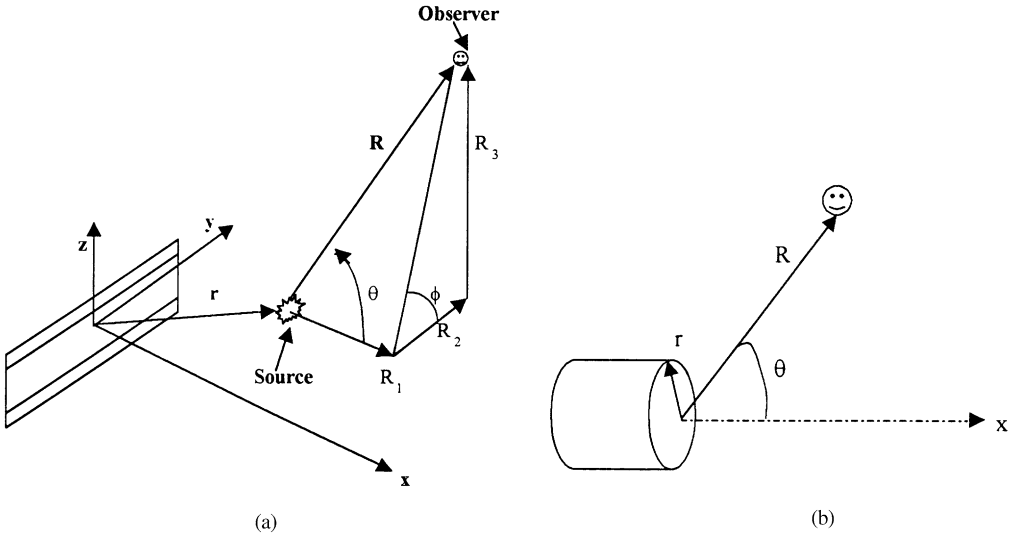

Figure 1. Reference co-ordinate system: (a) non-axisymmetric engine and (b) axisymmetric engine.

model that accounts for both k/ε and k/Pr is introduced. The various results are compared to farfield acoustic measurements. This study is restricted to the mixing noise only and, though important, no attempt is made at including the effects of heat sources and shocks. In the next section, the mathematical model is derived, followed by the computational methodology used. The various mean flow and acoustic radiation results are then discussed. Finally, some concluding remarks are given.

2. MATHEMATICAL MODEL

The starting point of this model is the farfield approximation of the Lighthill acoustic analogy, which can be written as

$$p(\mathbf{R}, t) = \frac{R_i R_j}{4\pi C_\infty^2 R^3} \int_V \left[\frac{\partial^2 T_{ij}}{\partial t^2} \right] \mathrm{d}^3 \mathbf{y}, \tag{1}$$

where T_{ij} is the Lighthill stress tensor given by

$$T_{ij} = \rho v_i v_j + \tau_{ij} + (\pi - C_\infty^2 \rho)\delta_{ij}. \tag{2}$$

In equation (2), the dominant term is the unsteady momentum flux $\rho v_i v_j$, τ_{ij} is the viscous compression stress tensor, π the local pressure, ρ the density, C_∞ the ambient speed of sound, v_i the velocity, and δ_{ij} is the Kronecker symbol ($= 0$ if $i \neq j$, $= 1$ if $i = j$). The notation "[ ]" in equation (1) denotes evaluation at the retarded time, $\tau = t - \mathbf{R}/C_\infty$. On retaining the dominant term [17], i.e., $\rho v_i v_j$, Mani *et al.* [10] showed that the mean square pressure $\overline{p^2}$ radiated in the observer direction $(\mathbf{R}, \theta)$ in polar co-ordinates (see Figure 1) can be written as

$$\overline{p^2}(R, \theta, \Omega) = \int_V \Psi(a_{xx} + 4a_{xy} + 2a_{yy} + 2a_{yz}) \mathrm{d}^3 r, \tag{3}$$

where

$$\Psi = \frac{I(\Omega)}{16\pi^2 R^2 C_\infty^4}\left(\frac{\rho_\infty}{\rho}\right)^2\left(\frac{C_\infty}{C}\right)^2 (1 - M\cos\theta)^{-2}(1 - M_c\cos\theta)^{-1}. \tag{4}$$

In equation (4), $I(\Omega)$ is the spectrum given by

$$I(\Omega) = c_l^3 \rho^2 k^{7/2}(\Omega\tau_0)^4 \mathrm{e}^{-1/8(\Omega\tau_0)^2}, \tag{5}$$

where Ω is the source frequency, which is related to the observed frequency by [10, 12]

$$\Omega = 2\pi f\sqrt{(1 - M_c\cos\theta)^2 + (c_d k^{1/2}/C_\infty)^2}. \tag{6}$$

M_c is the convection Mach number

$$M_c = \tfrac{1}{2}M + c_c M_j \tag{7}$$

and M is the local Mach number with M_j being the nozzle exit Mach number and (c_c, c_d) empirical constants. In equation (5), c_l is an empirical constant linked to the length scale

$$L = c_l k^{1/2}\tau_0 \tag{8}$$

with τ_0 being the characteristic time delay which determines the minimum significant correlation in a moving reference frame.

In equation (3), the directivity factors $(a_{xx}, a_{xy}, a_{yy}, a_{yz})$ have different forms depending on the location of the source, the velocity and temperature profiles in the vicinity of the source. These factors depend explicitly on a shielding function g^2 that has the form

$$g^2(r) = \frac{(1 - M\cos\theta)^2 (C_\infty/C)^2 - \cos^2\theta}{(1 - M_c\cos\theta)^2}. \tag{9}$$

Depending on the location and the shape of the profiles (i.e., velocity and temperature), the function g^2 may have both positive and negative regions in space. When a negative region exists, fluid shielding of the source is possible. The directivity factors are given by

$$a_{xx} = \frac{\cos^4\theta}{(1 - M_c\cos\theta)^4}\beta_{xx}, \qquad a_{xy} = \frac{g_0^2\cos^2\theta}{2(1 - M_c\cos\theta)^2}\beta_{xy}, \tag{10a, b}$$

$$a_{yy} = \tfrac{3}{8}g_0^4\beta_{yy}, \qquad a_{yz} = \tfrac{1}{8}g_0^4\beta_{yz}, \tag{10c, d}$$

where g_0^2 is the value of $g^2(r)$ at the source radius $r = r_0$. The shielding coefficients $(\beta_{xx}, \beta_{xy}, \beta_{yy}, \beta_{yz})$ depend on the location of the source [10].

In equations (5) and (8), a characteristic time delay, τ_0, was introduced. The most widely used value for this time scale is

$$\tau_{0,\varepsilon} = c_t^\varepsilon \frac{k}{\varepsilon}. \tag{11}$$

In this paper, two more time scales are considered,

$$\tau_{0,U} = \left(c_t^U \frac{\partial U}{\partial n} \right)^{-1} \tag{12}$$

and

$$\tau_{0,Pr} = c_t^{Pr} \frac{k}{Pr}. \tag{13}$$

In equation (12), $(\partial U/\partial n)$ is given by

$$\frac{\partial U}{\partial n} = \sqrt{\left(\frac{\partial U}{\partial y}\right)^2 + \left(\frac{\partial U}{\partial z}\right)^2}. \tag{14}$$

The production of the turbulent kinetic energy, Pr in equation (13) is written as

$$Pr = \frac{\mu_t}{\rho}[2(u_x^2 + v_y^2 + w_z^2) + (u_y + v_x)^2 + (v_z + w_y)^2 + (w_x + u_z)^2 - \tfrac{2}{3}(u_x + v_y + w_z)^2], \tag{15}$$

where μ_t is the turbulent viscosity, and (u, v, w) are the plume velocity components in the (x, y, z) directions respectively. In the extended version of the $(k - \varepsilon)$ turbulence model [18] used in the current CFD computation, the source term in the dissipation rate equation is given by

$$S_\varepsilon = \rho[C_1 Pr(\varepsilon/k) - C_2 \varepsilon(\varepsilon/k) + C_3 Pr(Pr/k)], \tag{16}$$

which shows the presence of two time scales: k/ε and k/Pr. Therefore, an acoustic model that accounts for radiation from both time scales is proposed. This model determines the far field mean-square-pressure as the average of the mean-square-pressure given by the individual time scales following

$$\overline{p^2} = \tfrac{1}{2}[\overline{p_\varepsilon^2} + \overline{p_{Pr}^2}], \tag{17}$$

where $\overline{p_\varepsilon^2}$ and $\overline{p_{Pr}^2}$ are associated with $\tau_{0,\varepsilon}$ and $\tau_{0,Pr}$ of equations (11) and (13) respectively. The model defined by equation (17) is referred to as the "dual time-scale" model.

3. METHOD OF SOLUTION

3.1. MEAN FLOW COMPUTATION

In one computation, the Reynolds-averaged Navier–Stokes (RANS) equations are integrated over a domain 2.5 times the length of the X-33 vehicle of 25 m. The main CFD code used is known as FDNS [19]. The code uses a second order finite difference scheme to discretize the diffusion fluxes and source terms of the governing equations. The convective terms are discretized using a second order total-variation-diminishing difference scheme. Details about the grid refinement techniques used and the treatment of the various

boundary conditions and source terms can be found in reference [20]. An extended ($k - \varepsilon$) turbulence model is used to describe the turbulence. The second computation was carried for a Mach 2, axisymmetric hot jet using the standard ($k - \varepsilon$) turbulence model. The number of points used in the streamwise and radial directions is 141 and 269 respectively.

3.2. ENGINE NOISE COMPUTATION

Using the CFD plume results, integration of equation (3) over the entire plume volume is carried out. In the case of the X-33 engine plume, the geometry of the engine is not axisymmetric, therefore integration must be carried out in all the three directions. This is done by first integrating each cross-section (i.e., in the (y, z) directions), followed by integration in the streamwise direction (i.e., x direction). In equation (7), the jet Mach number, M_j, is needed to compute the convection Mach number, M_c. For the axisymmetric case, it is taken to be 2; while for the non-axisymmetric case, it is obtained by averaging the local Mach number, M, over the engine exit plane.

4. RESULTS AND DISCUSSIONS

4.1. MEAN FLOW RESULTS

The freestream parameters used in both computations are: density $\rho_\infty = 1{\cdot}2\ \mathrm{kg/m^3}$, temperature $T_\infty = 300$ K, Mach number $M_\infty = 0$. Figure 2 shows the lateral average of the non-dimensional turbulent kinetic energy profiles as a function of the non-dimensional vertical distance at three different downstream locations for the X-33 engine plume. The figure shows the asymmetry of the profiles caused by differences in geometry between the upper and lower surfaces. Figure 3 shows the variation of the vertical average

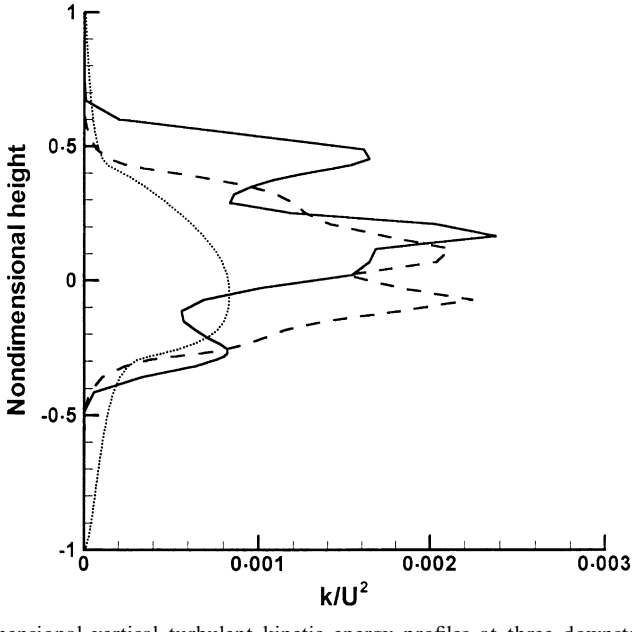

Figure 2. Non-dimensional vertical turbulent kinetic energy profiles at three downstream locations: ——, nozzle exit (0 m); – – – –, 3·3 m; ·····, 20 m (non-axisymmetric engine, X-33).

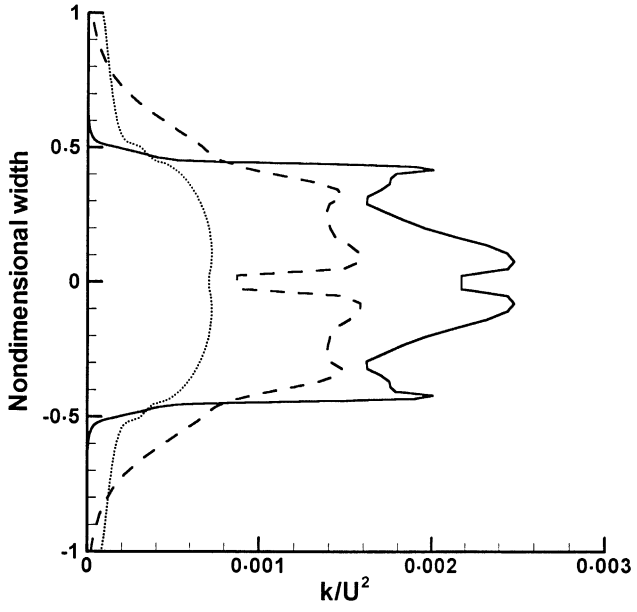

Figure 3. Non-dimensional lateral turbulent kinetic energy profiles at three downstream locations: ——, nozzle exit (0 m); – – – –, 3·3 m; ·····, 20 m (non-axisymmetric engine, X-33).

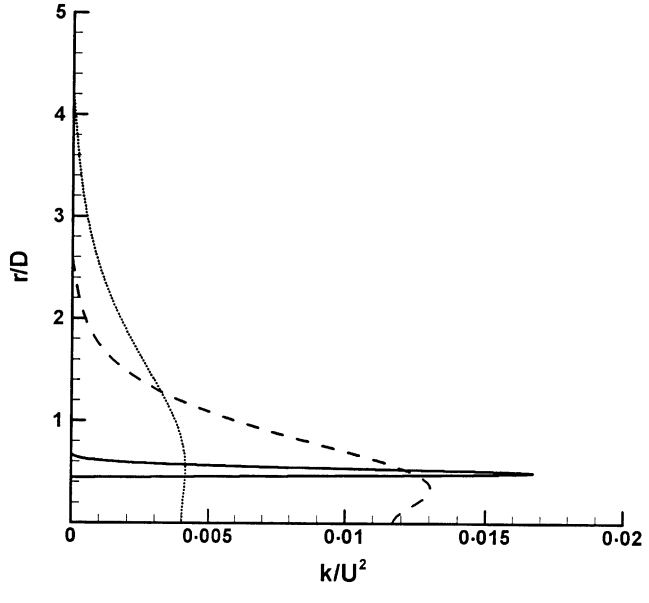

Figure 4. Non-dimensional turbulent kinetic energy profiles at three downstream locations: ——, 1 m; – – – –, 15 m; ·····, 30 m (axisymmetric jet).

of the turbulent kinetic energy with the lateral distance at the same three downstream locations and for the same engine. As expected, the profiles are symmetrical. For the axisymmetric jet, Figure 4 shows the non-dimensional turbulent kinetic energy profile as a function of the non-dimensional radial distance at three different downstream locations.

A major difference between the turbulent kinetic energy profiles of the X-33 engine plume and the axisymmetric jet is the presence of a single peak in the latter case and several peaks in the X-33 case. The lateral and vertical directions (in the X-33 case) are non-dimensionalized with the width and height of the engine, which are 2·24 and 1·07 m, respectively; whereas the radial direction (in the axisymmetric case) is non-dimensionalized by the jet diameter $D = 1{\cdot}0$ m.

4.2. ENGINE NOISE RESULTS

The first task to be performed is to select the various empirical constants of the model (c_c, c_d, c_l, c_t^U, c_t^ε, c_t^{Pr}). For the X-33 engine plume, this is achieved by using a measured spectrum in 1/3-octave frequency at a fixed observer location. Several measurements are made on the ground at a radius of 90 m from the test stand and at various angular locations. Because of the experimental set-up, the 90° location is chosen for calibration of the empirical constants. Figure 5 shows a comparison between the measured and calculated spectra using the various time scales. These results are obtained with the following set of empirical constants: $c_c = 0{\cdot}27$, $c_d = 0{\cdot}55$, $c_t^U = 0{\cdot}08$, $c_t^{Pr} = 0{\cdot}4$, $c_t^\varepsilon = 0{\cdot}045$ and $c_l = 1{\cdot}13$. The measured overall sound pressure level (OASPL) at the 90° location is also used in choosing the constants. The figure shows that the spectrum obtained using $\tau_{0,\varepsilon}$ as the time scale gives a poor agreement with the measurement at low frequencies. The calculated spectra using $\tau_{0,U}$ and $\tau_{0,Pr}$ as time scales show a better agreement with the measured spectrum. Both spectra obtained using these two time scales show the presence of a low- and a high-frequency peak, which is in good agreement with the measurement. This is not the case for the spectrum obtained using $\tau_{0,\varepsilon}$ as the time scale. Among the three time scales used, the best agreement is obtained using $\tau_{0,Pr}$. When the farfield acoustic radiation is obtained using both $\tau_{0,\varepsilon}$ and $\tau_{0,Pr}$ ("dual time-scale" model) through equation (17), the agreement

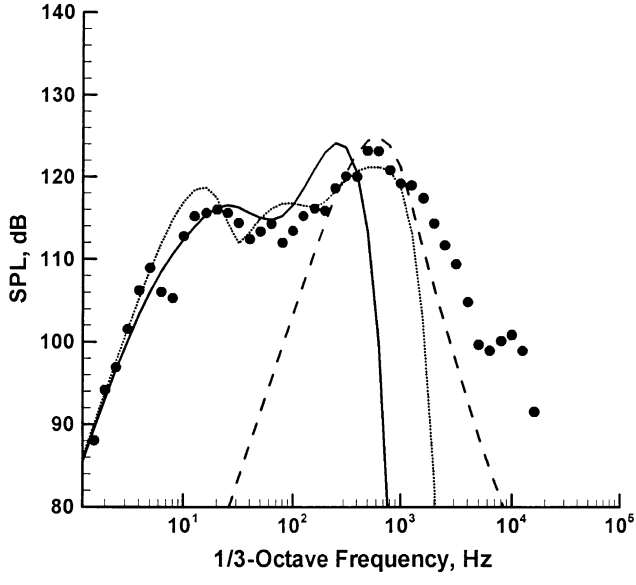

Figure 5. Comparison of the computed and measured spectrum at a farfield location 90 m from the test stand and at 90° angle with the engine axis: – – – –, computed with $\tau_{0,\varepsilon}$; ·····, computed with $\tau_{0,Pr}$; ——— computed with $\tau_{0,U}$; ●, measured (non-axisymmetric engine, X-33).

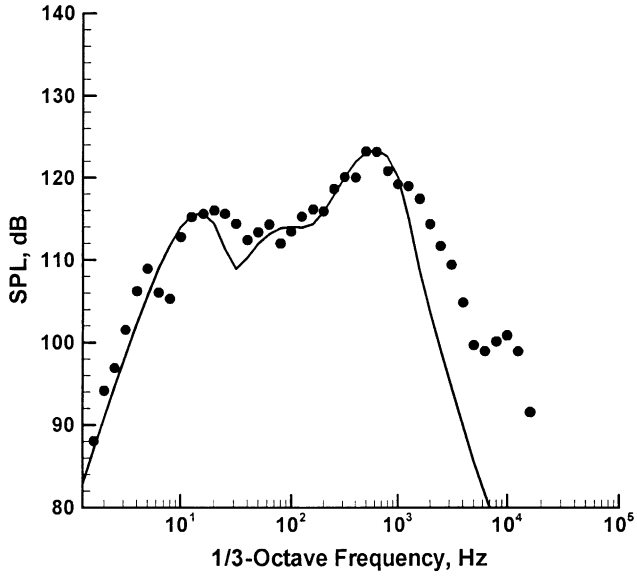

Figure 6. Comparison of the computed and measured spectrum at a farfield location 90 m from the test stand and at 90° angle with the engine axis: ——, computed using equation (17); ●, measured (non-axisymmetric engine, X-33).

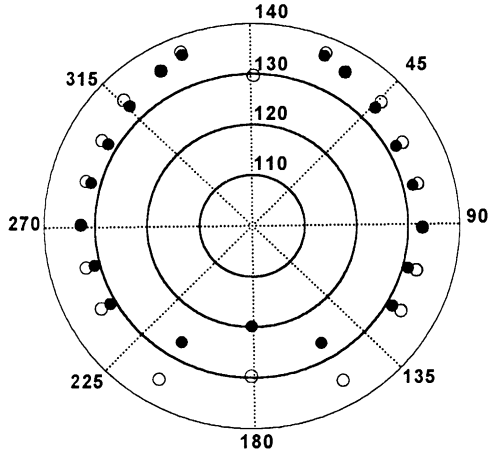

Figure 7. Comparison of the computed and measured sound pressure level at various angular locations with respect to the test stand: ●, measured; ○, computed (non-axisymmetric engine, X-33).

between the measured and calculated spectrum is significantly improved as shown in Figure 6. This better agreement is believed to be due to the fact that the turbulence model used accounts for both these time scales in the source term of the dissipation rate equation (16). Using the set of empirical constants given above, the overall sound pressure level at various angular locations around the test stand is calculated and compared to the measurements in Figure 7. The calculated results are in good agreement with the measurements over most angular locations except near 180°, where a wall exists between the engine plume and the microphone, which is not simulated in the computation.

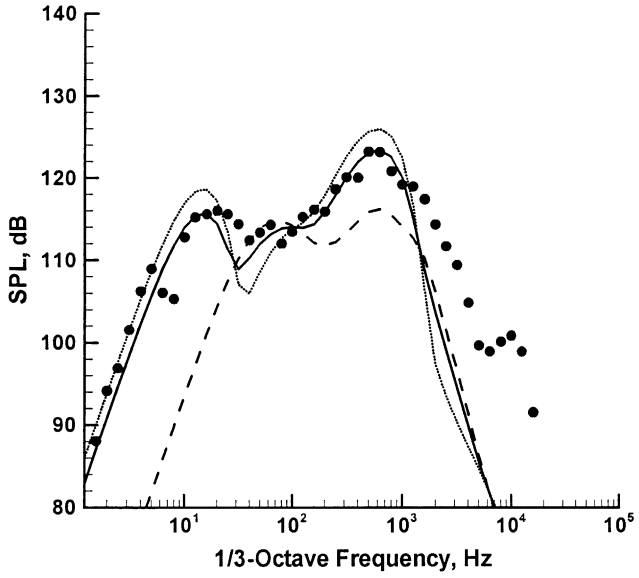

Figure 8. Relative contribution of the lateral and vertical engine directions to the total farfield engine noise spectrum: – – – – –, lateral direction; ·····, vertical direction; ——, total computed spectrum; ●, total measured spectrum.

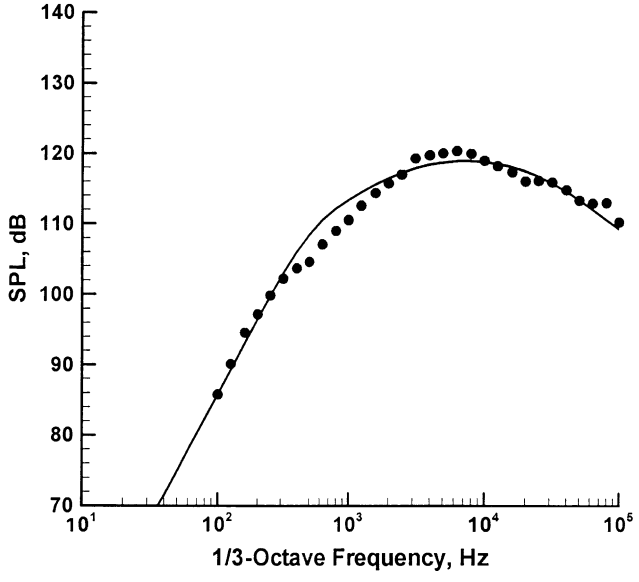

Figure 9. Comparison of the computed and measured spectrum at a farfield location 110 m from the engine exit plane and at 73° angle with the engine axis: ——, computed using equation (17); ●, measured (axisymmetric jet).

Figure 8 shows the relative contribution of the lateral and vertical directions of the engine plume to the calculated overall spectrum (the "dual time-scale" model is used in all the calculations). The measured spectrum is also shown for completeness. The figure shows that the vertical direction contributes the most to the overall spectrum. The contribution of the lateral direction is significant only in the region between the high- and low-frequency peaks.

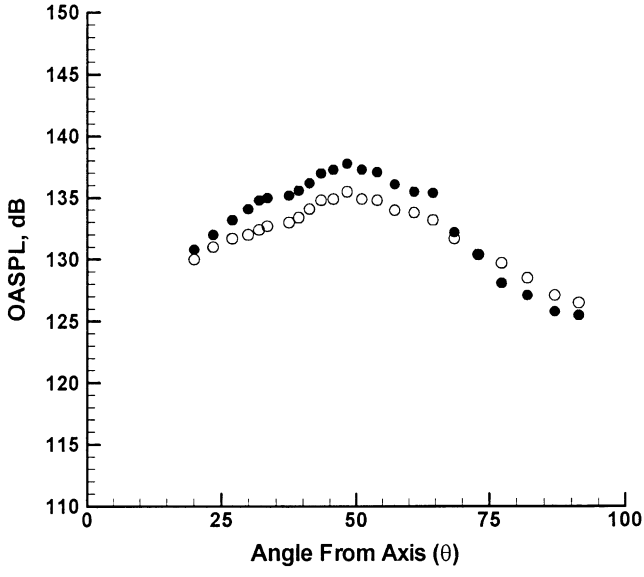

Figure 10. Comparison of the computed and measured sound pressure level at various angular locations with respect to the test stand: ●, measured; ○, computed (axisymmetric jet).

For the axisymmetric jet, a new set of empirical constants is obtained using the same approach as above, $c_c = 0{\cdot}492$, $c_d = 0{\cdot}55$, $c_t^U = 0{\cdot}04$, $c_t^{Pr} = 0{\cdot}03$, $c_t^\varepsilon = 0{\cdot}07$ and $c_l = 1{\cdot}0$. The experimental data used are those obtained by Seiner [21]. Figure 9 shows a comparison between a measured and computed spectrum at a radius of 110 m and an angle of 73° with the axis of the jet. The dual time-scale model given by equation (17) is used to compute the spectrum. Good agreement is obtained between the measured and computed spectrum as the figure shows. The OASPL as a function of the angle with the jet axis (known as directivity) is shown on Figure 10. The same empirical constants are used at all angles. The figure shows reasonable agreement between the measured and computed directivity.

5. CONCLUDING REMARKS

A semi-empirical acoustic radiation model is derived from the Lighthill acoustic analogy to study the noise radiated by an engine plume. Axisymmetric and non-axisymmetric engines are considered. Various time scales are tested and the results show that a "dual time-scale" model that accounts for radiation using $\tau_{0,\varepsilon}$ and $\tau_{0,Pr}$ as time scales, gives the best agreement with the measurements. For the non-axisymmetric engine case, the widely used $\tau_{0,\varepsilon}$ time scale gave a poor agreement with the measurement, whereas $\tau_{0,Pr}$ and $\tau_{0,U}$ performed better. An important conclusion of this study is the existence of a strong relationship between the turbulence model being used and the acoustic radiation model. It is therefore recommended that the choice of the time scale for the acoustic radiation model be obtained from the turbulence model being used.

ACKNOWLEDGMENTS

The first author would like to acknowledge the support of NASA Marshall Space Flight Center under the SBIR contact ASRI-NAS8-01009-01 monitored by Tom Nesman.

REFERENCES

1. M. J. LIGHTHILL 1952 *Proceedings of the Royal Society Series A* **211**, 564–587. On sound generated aerodynamically: I. General theory.
2. M. J. LIGHTHILL 1954 *Proceedings of the Royal Society Series A* **222**, 1–32. On sound generated aerodynamically: I. Turbulence as a source of sound.
3. H. S. RIBNER 1969 *Journal of Fluid Mechanics* **38**, 1–24. Quadrupole correlations governing the pattern of jet noise.
4. H. S. RIBNER 1958 *Journal of the Acoustical Society of America* **31**, 245–246. On the strength distribution of noise sources along a jet.
5. H. S. RIBNER 1963 *Journal of the Acoustical Society of America* **35**, 614–616. On spectra and directivity of jet noise.
6. J. E. FFOWCS WILLIAMS 1969 *Annual Review of Fluid Mechanics* **1**, 197–222. Hydrodynamics noise.
7. J. E. FFOWCS WILLIAMS 1969 *Annual Review of Fluid Mechanics* **9**, 447–468. Aeroacoustics.
8. M. E. GOLDSTEIN 1984 *Annual Review of Fluid Mechanics* **16**, 263–285. Aeroacoustics of turbulent shear flows.
9. C. K. W. TAM 1995 *Annual Review of Fluid Mechanics* **27**, 17–43. Supersonic jet noise.
10. R. MANI, E. J. STRINGAS, J. C. F. WANG, T. F. BALSA, P. R. GLIEBE and R. A. KANTOLA 1977 Task 2, 1977, FAA-RD-76-79-II. High velocity jet noise source location and reduction.
11. J. E. FFOWCS WILLIAMS 1963 *Philosophical Transactions of the Royal Society of London Series A* **255**, 469–503. The noise from turbulence convected at high speed.
12. A. FRENDI T. E. NESMAN and T.-S. WANG 2001 *American Institute of Aeronautics and Astronautics Journal* **39**, 1485–1492. Computational and experimental study of the linear aerospike engine noise.
13. A. KHAVARAN, E. A. KREJSA and C. M. KIM 1992 *AIAA*, Paper 92-0500. Computation of supersonic jet mixing noise from an axisymmetric CD nozzle using $(k - \varepsilon)$ turbulence model.
14. V. FORTUNE and Y. GERVAIS 1999 *American Institute of Aeronautics and Astronautics Journal* **37**, 1055–1061. Numerical investigation of noise radiated from hot subsonic turbulent jets.
15. C. BAILLY, P. LAFON and S. CANDEL 1997 *American Institute of Aeronautics and Astronautics Journal* **35**, 1688–1696. Subsonic and supersonic jet noise predictions from statistical source models.
16. C. K. W. TAM and L. AURIAULT 1999 *American Institute of Aeronautics and Astronautics Journal* **37**, 145–153. Jet mixing noise from fine-scale turbulence.
17. M. E. GOLDSTEIN 1974 NASA SP-346, 103–159, Aeroacoustics.
18. Y. S. CHEN and S. W. KIM 1987 NASA CR-179204. Computation of turbulent flows using an extended $k - \varepsilon$ turbulence closure model.
19. Y. S. CHEN 1997 *Engineering Sciences Inc., ESI-TR*-97-01. *Huntsville, AL.* FDNS—a general purpose CFD code, Version 4.0.
20. T.-S. WANG 1999 *Journal of Spacecraft and Rockets* **36**, 777–783. Analysis of linear aerospike plume-induced X-33 base-heating environment.
21. J. M. SEINER, J. C. MANNING and M. K. PONTON *AIAA* Paper 86-1942. The preferred spatial mode of instability for a Mach 2 jet.